Remote Sensing of Environment 248 (2020) 111976

Contents lists available at ScienceDirect

Remote Sensing of Environment

journal homepage: www.elsevier.com/locate/rse

Two decades of settlement of Hong Kong International Airport measured with multi-temporal InSAR

Songbo Wu[a], Zefa Yang[a,b], Xiaoli Ding[a,*], Bochen Zhang[a,c], Lei Zhang[a], Zhong Lu[d]

[a] Department of Land Surveying and Geo-Informatics, The Hong Kong Polytechnic University, Hung Hom, KLN, Hong Kong
[b] School of Geosciences and Info-Physics, Central South University, Changsha, China
[c] MNR Key Laboratory for Geo-Environmental Monitoring of Great Bay Area, College of Civil and Transportation Engineering, Shenzhen University, 518060 Shenzhen, China
[d] The Roy M. Huffington Department of Earth Sciences, South Methodist University, Dallas, TX 75275, USA

ARTICLE INFO

Keywords:
Land reclamation
Settlement
MT-InSAR
HKIA

ABSTRACT

The Hong Kong International Airport (HKIA) was constructed on a platform mainly reclaimed from the sea. The platform has experienced some significant settlement since its operation in 1998 due mainly to consolidation of the materials used in the land reclamation. Although some studies have been carried out to measure the settlement with techniques such as Interferometric Synthetic Aperture Radar (InSAR), the past studies have each only covered some limited time periods. Therefore, a complete history of settlement since the operation of the Airport has never been available to aid the understanding of the spatiotemporal behavior of the land settlement. We attempt for the first time to make full use of most of the available SAR data from multiple SAR sensors (ERS-2, ENVISAT ASAR, COSMO-SkyMed (CSK), and Sentinel-1A) to generate a settlement time series of the HKIA over 1998–2018 with an improved multi-temporal InSAR technique. In order to fill the time gaps between the different SAR datasets, a settlement model is developed based on the InSAR measurements. The results reveal both the spatial and temporal variations of the land settlement. They also show for the first time that the accumulative settlement reaches up to 40 cm over the past two decades. The settlement is largely associated with the material types used in the landfill works and the underlying alluvial sediments as some earlier research has indicated, and the stages of the reclamation works. The results are validated through cross-validation between the datasets and with leveling and GPS measurements on the Airport platform.

1. Introduction

Hong Kong International Airport (HKIA) is one of the busiest passenger and cargo airports in the world. It was constructed on two existing islands, namely Chek Lap Kok and Lam Chau, and land reclamation from the surrounding water (Uiterwijk, 1994) as shown in Fig. 1. The reclaimed land accounts for about 75% of the airport area. Research has indicated that the HKIA platform has been subject to severe settlement since it started commercial operation in 1998, mainly due to soil consolidation, especially in the reclaimed areas (Uiterwijk, 1994; Plant et al., 1998; Plant and Oakervee, 1998; Tosen et al., 1998; Liu et al., 2001; Ding et al., 2004; Jiang and Lin, 2010). Such long-term and large-scale settlement may lead to damages to the infrastructures of the HKIA and threaten its normal operation. Therefore, it is important to monitor the settlement to assess its impacts.

Ground settlement can be measured with in-situ observations from traditional geodetic surveying techniques such as leveling and GPS. However, the spatial resolutions of these techniques are normally poor, and they are often labor-intensive. Interferometric Synthetic Aperture Radar (InSAR) is an active remote sensing technique and has become one of the most useful geodetic techniques for high-resolution large-area deformation measurements (e.g., Bamler and Hartl, 1998; Massonnet and Feigl, 1998; Rosen et al., 2000). To overcome the limitations of the conventional differential InSAR technique, such as decorrelation and atmospheric artifacts, multi-temporal InSAR (MT-InSAR) techniques have been developed to retrieve high-accuracy time-series of deformation (e.g., Ferretti et al., 2000; Berardino et al., 2002; Hooper et al., 2004; Kampes, 2006; Pepe and Lanari, 2006; Zhang et al., 2012; Costantini et al., 2014; Jiang et al., 2014).

Each of the existing InSAR studies on the settlement of the HKIA platform only covered a limited time period and the studies are not interconnected. Although the studies are very useful, they are unable to provide a full history of the spatiotemporal evolution of the settlement. For example, Liu et al. (2001) first retrieved the surface settlement of

* Corresponding author.
E-mail address: xl.ding@polyu.edu.hk (X. Ding).

https://doi.org/10.1016/j.rse.2020.111976
Received 13 June 2019; Received in revised form 26 June 2020; Accepted 2 July 2020

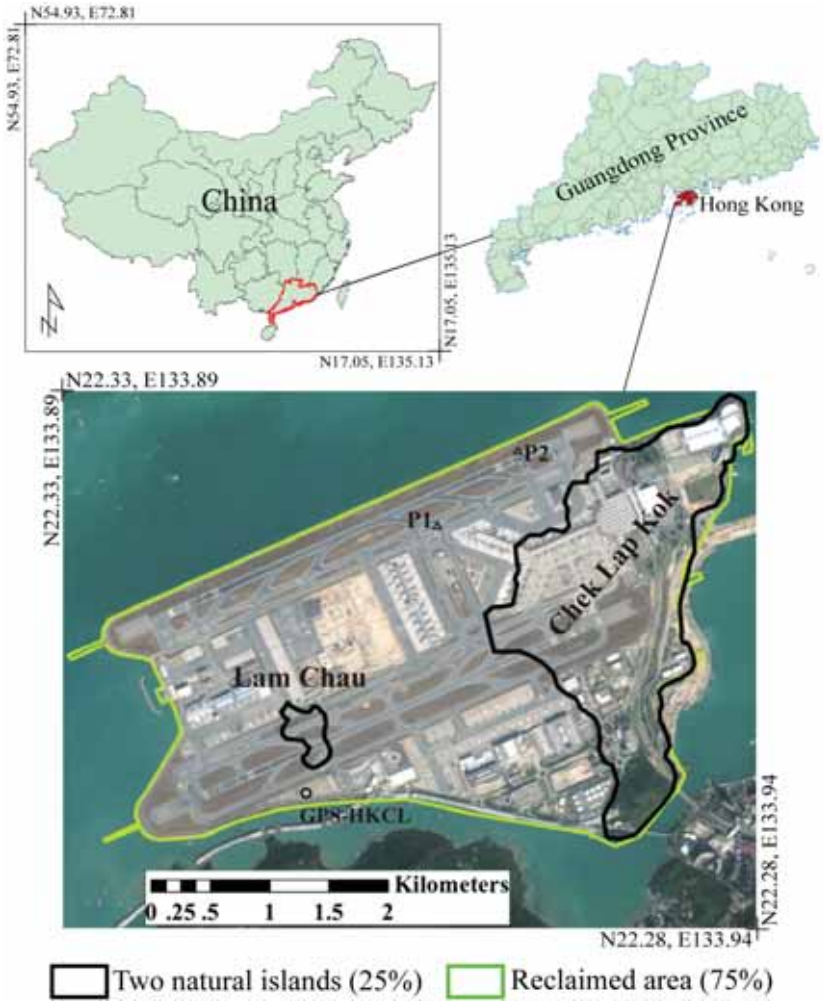

Fig. 1. The location of the HKIA. (Background image: Google Maps satellite image.)

the HKIA platform over 1996–1999 using two European Remote Sensing (ERS) images and concluded that the reclaimed area experienced significant settlement. Zhao et al. (2009, 2011) retrieved the time-series of settlement using ENVISAT images over 2006–2008. Jiang and Lin (2010) studied the settlement over 2003–2008 and found that the settlement of the southern runway was related to the thickness and properties of both the fill materials and the alluvial deposits. Sun et al. (2016, 2018) provided a time-series of ground deformation of the HKIA over 2008–2009 with TerraSAR-X Spotlight images and elaborated the characteristics of localized deformation of the HKIA. Ma et al. (2019) measured the ground deformation of the HKIA over 2015–2017 with CSK images and over 2013–2017 with Sentinel-1A images and validated the results with leveling measurements. It can be seen that these studies have covered disjointed time periods only. Further research is therefore required to provide an overall view of the settlement history of the HKIA and to better understand the factors impacting on the settlement.

We will in this study attempt to retrieve the temporally continuous settlement history of the HKIA over the past two decades (i.e., since its operation) using most of the available space-borne SAR images, i.e., ERS-2 (1998–2000), ENVISAT (2003 – 2010), CSK (2013–2017), and Sentinel-1A (2015–2018), with an improved MT-InSAR method (Wu et al., 2018). Since the SAR data does not cover the whole study period, a settlement model (Plant et al., 1998; Pepe et al., 2016) will be developed to bridge the time gaps.

2. Study area and datasets

2.1. HKIA and its reclamation history

The HKIA is located on the western side of the Hong Kong Special Administrative Region (Fig. 1) and its platform covers an area of approximately 12.55 km^2. Around 25% of the Airport platform was based on two existing islands, namely Chek Lap Kok and Lam Chau as shown in Fig. 1, and the remaining 75% of the area was reclaimed from the sea. The construction of the HKIA platform took about 3 years, from December 1992 to June 1995 (Plant et al., 1998). The main construction stages are shown in Fig. 2. The construction first took place at the Chek Lap Kok island. The southern and northern parts of the platform were finished in 1994 and 1995, respectively. The parts to the west of the Lam Chau island and to the north-west of the Chek Lap Kok island were constructed last along the southern and northern parts of the platform.

The staged construction approach allowed two work components, marine and civil, to be implemented simultaneously in different areas during the reclamation works (Plant et al., 1998). The marine component involved seawall construction, mud dredging, and filling with marine sand. The civil component included blasting, excavation, filling, and geotechnical works. The filling works (both marine and land) were implemented with seven types of landfill materials as described in Table 1.

The thickness of the filling materials gradually decreased from north to south, varying from 29 m to 3 m (Plant et al., 1998; Jiang and Lin,

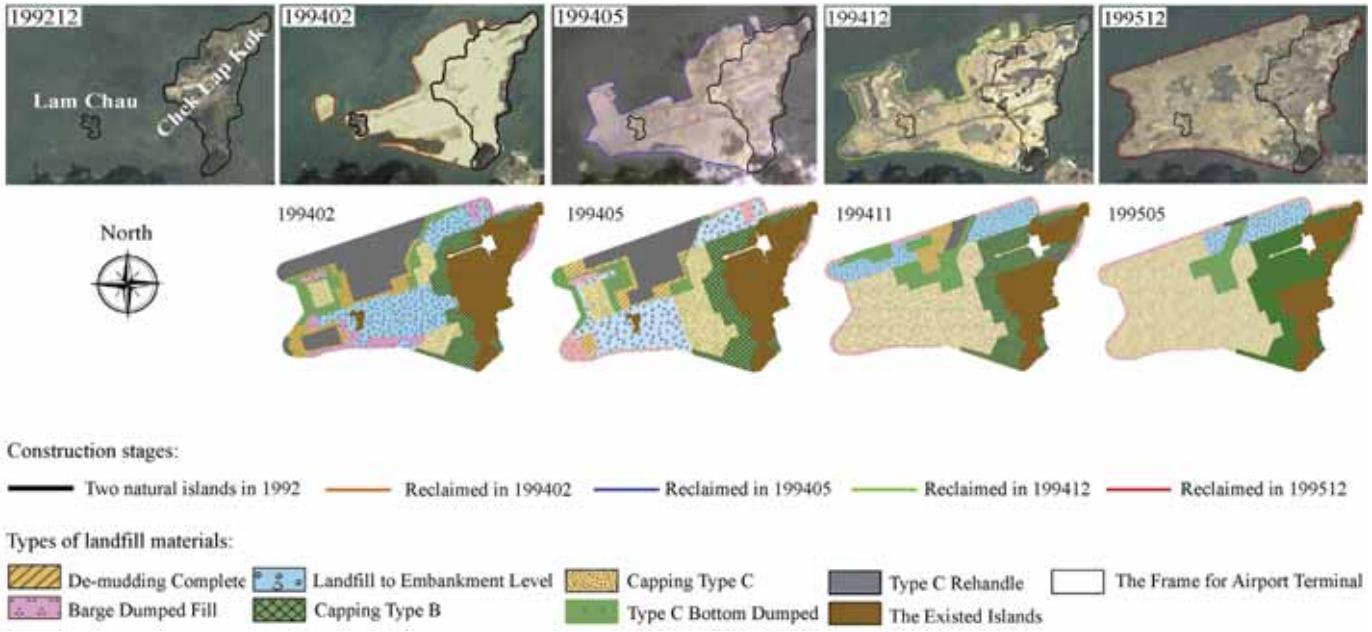

Fig. 2. Construction stages of the HKIA platform and types of landfill materials. (Background image: Google Maps satellite image.)

2010). According to the intended use of the airport platform and the quantities of available materials, the distribution of the filling materials varied spatially. For instance, the southern runway area consisted of Type A materials which are "liquefaction-proof". The entire HKIA platform was capped with Type B and/or Type C materials to allow the construction of, e.g., tunnels beneath the runways.

2.2. Datasets

Multi-sensor space-borne SAR satellite datasets over the HKIA area were collected for measuring the settlement of the HKIA platform, as outlined in Table 2. The areas of coverage of the SAR datasets are shown in Fig. 3(a). The acquisition dates of the images are indicated in Fig. 3(b). A LiDAR digital elevation model (DEM) provided by the Hong Kong Government with a spatial resolution of 10 m is also available for geocoding the calculated settlement. Leveling measurements on two benchmarks, P1 and P2 shown in Fig. 1, were collected to validate the InSAR results. GPS measurements at 13 continuous GPS (CGPS) stations (see Fig. 3(a)) were also collected from the Nevada Geodetic Laboratory (Blewitt et al., 2018). One GPS station, HKCL, located on the reclaimed land will also be used to validate the InSAR results. Google Maps images of the HKIA are used as the background for displaying the results.

3. Methodology and results

3.1. Methodology

3.1.1. Interferometric processing

All SAR data used in the study was preprocessed with GAMMA software (Werner et al., 2000). The preprocessing mainly includes SAR image extraction and co-registration, interferogram generation, flat-earth phase removal, and geolocation.

3.1.2. Retrieval of time-series deformation

A MT-InSAR method (Wu et al., 2018) is first used to process the individual SAR data series to obtain time series of line-of-sight (LOS) deformation measurements (see Fig. 3(b) for time period covered by each SAR dataset). It is assumed that a set of N co-registered SAR images from a data series is used to generate M interferograms. Only interferograms whose spatial and temporal baselines are within given thresholds are used (see Fig. S1 in the Supplementary Materials for the baseline thresholds used). The interferograms are also inter-connected. We divide the area covered by each SAR data series into small overlapped patches and connect all the pixel pairs within each patch to generate an arc network with very high redundancy. The differential phases between the pixel pairs are considered the observations. For the i-th arc, the $M \times 1$ observation vector is represented by $\Delta\phi_i^{arc}$. The unwrapped interferometric phases between successive SAR acquisitions, $\Delta\varphi_i^{arc}$ are considered as unknowns. The observation equations for an arc are

$$\mathrm{B}\,\Delta\varphi_i^{arc} = \Delta\phi_i^{arc} \tag{1}$$

where B represents a $M \times (N-1)$ coefficient matrix that contains only 0 and 1, depending on the interferograms generated. For instance, if the m-th interferogram spans k ($k \in 1, 2, \ldots N-1$) successive acquisition intervals, only the corresponding k columns of the m-th row are equal to 1. Matrix B should be full rank and the least squares solution of Eq. (1) is $\Delta\varphi_i^{arc} = (\mathrm{B}^{\mathrm{T}}\mathrm{B})^{-1}(\mathrm{B}^{\mathrm{T}}\Delta\phi_i^{arc})$ when considering the observations are of

Table 1
Landfill materials for constructing the HKIA platform (Plant et al., 1998).

Type	Material components
Type A:	*As-blasted rock with a maximum size of 2000 mm and a fines limit of 50%.*
Type B:	*Excavated soil or rock with a maximum size of 300 mm.*
Type A/B:	*A mixture of Type A and Type B fill which was not included in the original Site Preparation Contract (SPC) specification.*
Type C:	*Sandfill with a fines content of 20% or less, generally placed wet and won from marine sources.*
Type D:	*Rockfill for seawalls, not coarser than Type A nor finer than Type E.*
Type E:	*Rockfill as blasted, crushed, and/or screened as necessary with a maximum size limit of 150 mm and intended for use in areas to be re-excavated or piled later.*
Type F:	*Completely decomposed granite (CDG) with a maximum size limit of 200 mm*

Table 2
SAR datasets used for the study.

Sensors	ERS-2	ENVISAT ASAR			CSK	Sentinel-1A
Orbit	Descending	Ascending 25	Ascending 297	Descending 175	Descending	Ascending
Time period	19980621–20000521	20070613–20100428	20070423–20090914	20030406–20100926	20131004–20171120	20150615–20180623
No. of scenes	6	19	19	34	42	80

equal weight. The least squares residuals can be estimated with $\Delta\varphi_i^{res} = \Delta\phi_i^{arc} - B(B^TB)^{-1}(B^T\Delta\phi_i^{arc})$.

When all the arcs are considered, the solution can be obtained based on an extension of the TCP-InSAR framework (e.g., Zhang et al., 2011; Zhang et al., 2012). We examine the least squares residuals and remove observations with large residuals in the next iteration of the solution. Large residuals may be caused by strong noise and/or phase ambiguities. In analyzing the residuals, each residual is compared with the mean absolute residual of the corresponding arc $E(\Delta\varphi_i^{res})$ plus the standard deviation σ_{arc} of the residual. The observation will be removed if its residual satisfies

$$|\Delta\varphi_i^{res}| > E(\Delta\varphi_i^{res}) + \sigma_{arc} \quad (2)$$

$$\sigma_{arc}^2 = 2\sigma_{point}^2$$

where σ_{point} represents the standard deviation of the phase noise of a typical coherent point. For instance, we can expect that the standard deviation of the phase noise of a coherent point to be less than 0.45 rad for a C-band SAR image (i.e., $\sigma_{point} = 0.45$ radians) and thus $\sigma_{arc} \approx 0.636$ radians.

Unwrapped phase non-closures of triangular arc loops are also used to detect arcs that likely have phase ambiguities (Hussain et al., 2016). The unwrapped phases of coherent points can be obtained by spatial

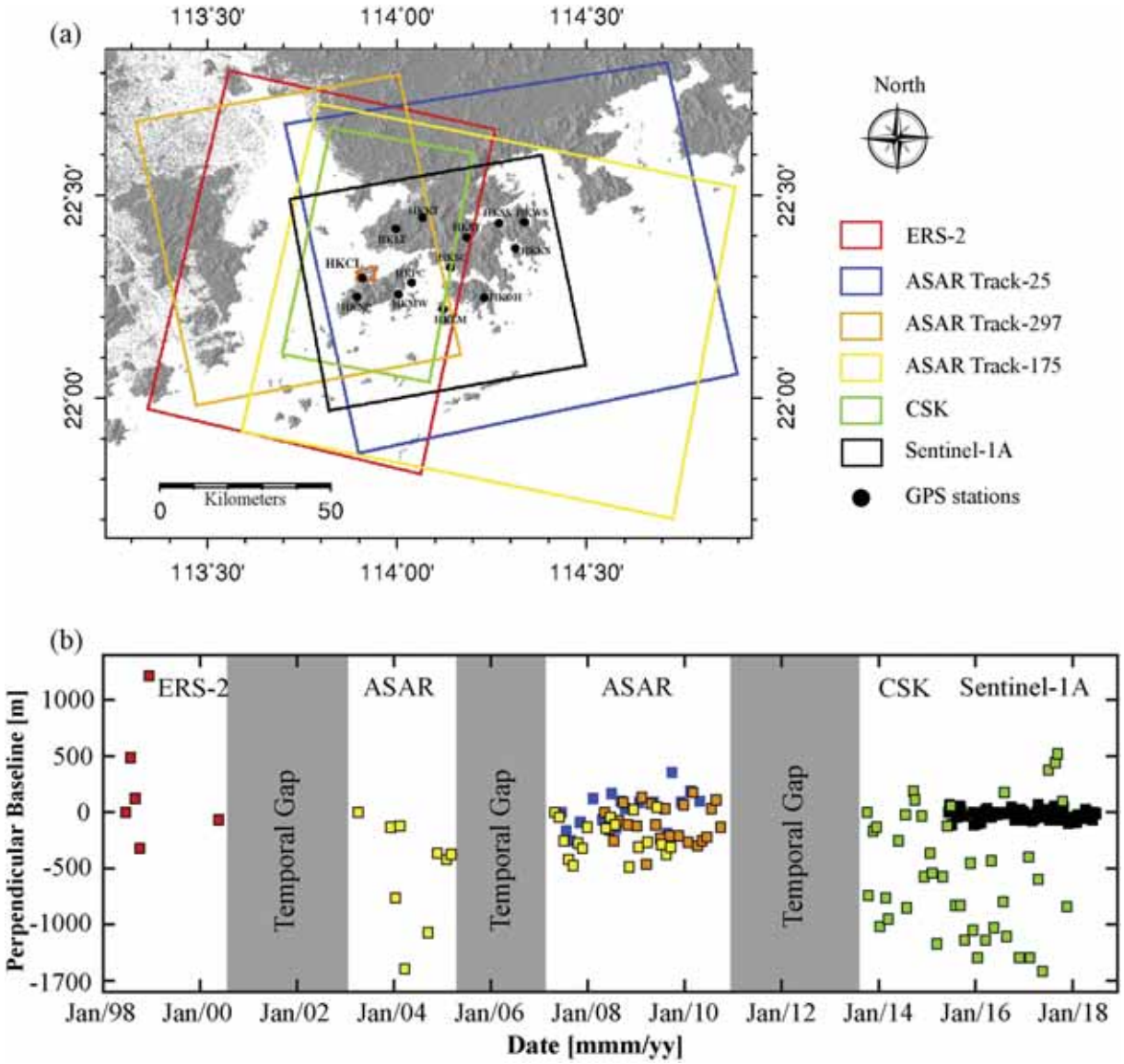

Fig. 3. (a) Areas of coverage of SAR images used in the study. (b) Acquisition dates and perpendicular baselines of SAR data (with respect to the earliest SAR image in each series). The black dots in (a) indicate the locations of the 13 continuous GPS stations used in the data analysis. The gray areas in (b) represent the time gaps between the SAR datasets.

integration from a given reference point (Ferretti et al., 2001; Kampes, 2006). In this study, we chose an area near the terminal building on the Chek Lap Kok island (see Fig. 6) as the common reference area for all the datasets, and each set of results from the different SAR datasets is referred to the point with the highest amplitude dispersion index (ADI) in the reference area. Long-wavelength signals such as those related to orbital errors and atmospheric delays are removed using the joint TCP-InSAR model (e.g., Zhang et al., 2014; Liang et al., 2018). The DEM phases are estimated based on the unwrapped phases (Berardino et al., 2002; Fattahi and Amelung, 2013). The deformation time series in the LOS direction for each point is then obtained with respect to the earliest SAR image within the data series. Different from other commonly used algorithms (e.g., PSI, SBAS, and StaMPS), the method is a pixelwise estimator and it integrates coherent point selection and phase unwrapping into one step. It can estimate unwrapped phases in successive temporal intervals directly from multi-master wrapped interferograms. More importantly, assumption of a deformation model is not required in the processing chain as it takes the unwrapped phase vectors as unknowns (Wu et al., 2018).

3.1.3. Thermal dilation correction

The area over the HKIA is covered by various infrastructures such as buildings. Thermal dilation of the infrastructures may bias the deformation retrieved (Monserrat et al., 2011; Chang, 2015; Niu et al., 2015). Considering that thermal dilation is related to air temperature, we use the daily mean air temperature on the SAR acquisition date to correct the effect for data acquired on that day,

$$\delta\varphi_{los} = \begin{cases} \delta\varphi - \delta\widehat{\varphi}_{TD}, \ correlation\ coeficient \geq \varepsilon \\ \delta\varphi, \ correlation\ coeficient < \varepsilon \end{cases} \quad (3)$$

where $\delta\varphi_{los}$ is the thermal dilation corrected phase; $\delta\varphi$ is the unwrapped DEM-compensated phase of a coherent point; $\delta\widehat{\varphi}_{TD}$is the estimated thermal dilation phase, and ε is a threshold for the correlation coefficient (0.5 in this case as determined based on trial and error) between the temperature and the phase change.

3.1.4. Bridging temporal gaps between SAR datasets

The retrieved time series of LOS deformation from each SAR dataset is respect to the earliest acquisition date of that dataset. To retrieve the time-series of deformation over the two decades of operation of the airport, the LOS deformation observations are projected to vertical direction by assuming that the horizontal displacements are negligible as discussed in Section 4.2. We attempt to build a settlement model, f, based on the measurement results to describe the continuous temporal evolution of the settlement (Plant et al., 1998; Pepe et al., 2016),

$$\widehat{d}_v = \arg\min\{\|f - d_v\|_2\} \quad (4)$$

$$f(t, V, a, b) = V\frac{(t)^b}{(a)^b + (t)^b}$$

where d_v represents the settlement time-series relative to the first image of the SAR image in the time series; V denotes the vertical displacement vector at time t; and a and b are the shape parameters. Parameters V, a, and b are considered as unknowns to be estimated by best fitting between the model curve, f, and the settlement measurements, d_v. The data processing chain is shown in Fig. 4 below,

3.2. Results

805 interferograms whose spatiotemporal baselines are within the given thresholds are generated from the available SAR images. The images deployed and the baseline distributions of the interferograms are given in Table S1 and Fig. S1 of the Supplementary Materials. Multi-look operation is not carried out to retain the details of the ground deformation. Due to the rapid land cover changes during the airport construction, the topographic phase cannot be compensated exactly by using a common DEM. Instead, we use a DEM generated from LiDAR data to geocode the LOS deformation results, rather than compensating the DEM phase during MT-InSAR data processing. The estimated surface heights from the different SAR datasets are shown in Fig. S2 of the Supplement Materials.

3.2.1. Thermal dilation correction

Eq. (3) is used to correct the thermal dilation effect when the unwrapped phases of each SAR datasets are available. Fig. 5 shows the thermal dilation effect of a point on a building within the area from the CSK and Sentinel-1 SAR data, respectively. The results indicate that the thermal dilation effect is significant, with a correlation coefficient of 0.69 and 0.73 respectively for the CSK and Sentinel data. Before correcting the thermal dilation effect, the estimated deformation rates (red dashed lines) were − 4.1 mm/year and − 5.3 mm/year while they become −3.9 mm/year and − 4.5 mm/year, after the correction. The temporal evolution of the settlement (the black triangles) is better revealed after the thermal dilation correction has been made, which is important to the estimation of settlement time-series of the common points between the different datasets.

3.2.2. LOS deformation from SAR dataset

Fig. 6 shows the mean LOS deformation velocity maps derived from each of the SAR datasets (see Fig. 3(a)). As seen from Fig. 6(a), although the primary consolidation of the alluvial clay had been over 90% completed by the end of 1998 (Plant et al., 1998), the reclaimed areas still suffered from global residual settlement from 1998 to 2000. From 2003 to 2005, the deformation pattern tended to be localized. By the end of 2005, the maximum deformation reached a peak annual LOS velocity of greater than 25 mm. After 2005, the localized deformation started to slow down (see Fig. 6(c)–(g)). The deformation revealed was mainly along the two runways, particularly at the two ends and near the middle part of the northern runway, and the western end of the southern runway. The possible reasons for the deformation will be discussed further in Section 4.3. The localized areas of subsidence in Fig. 6(b)–(g) agree well largely with the findings in Sun et al. (2018) and Ma et al. (2019). The areas generated from the two islands remained fairly stable over the entire observation period. The variation in the point distribution and the quality of the results obtained from the different datasets may be caused by the different image resolutions, the change in the ground features during the study periods, and the quality of the images used.

3.2.3. Long-term settlement

Common points between the datasets are selected after re-sampling the InSAR results to a common georeferenced grid of 20 m resolution. A settlement model is finally determined based on Eq. (4). Fig. 7(a) shows the settlement velocity estimated from the model indicating that the HKIA platform suffered from very heterogeneous settlement. Four areas experienced most serious settlement, the areas that are adjacent to the Chek Lap Kok island on both the northwestern and southwestern sides, and the western ends of the two runways. The settlement time-series of some selected points as shown in Fig. 7(a) are given in Fig. 7(b)-(g). The curves represent the settlement estimated from the settlement model. The standard deviations of the residuals from the model fitting at these points are 5.22 mm, 4.10 mm, 4.43 mm, 4.37 mm, 5.26 mm, and 2.36 mm, respectively. Some measurements, such as some of those between 2003 and 2005 in Fig. 7(f) appear not to fit to the model as well as the others perhaps due to the effects of residual atmospheric delays and decorrelation. The results also clearly show that the settlement was all rapid at the beginning and then gradually slowed down. The maximum accumulated settlement reached 40 cm and it occurred at the area adjacent to the Chek Lap Kok island on the northwestern side. Since the overall long-term settlement is obtained based on the common points among all the SAR datasets, areas with severe

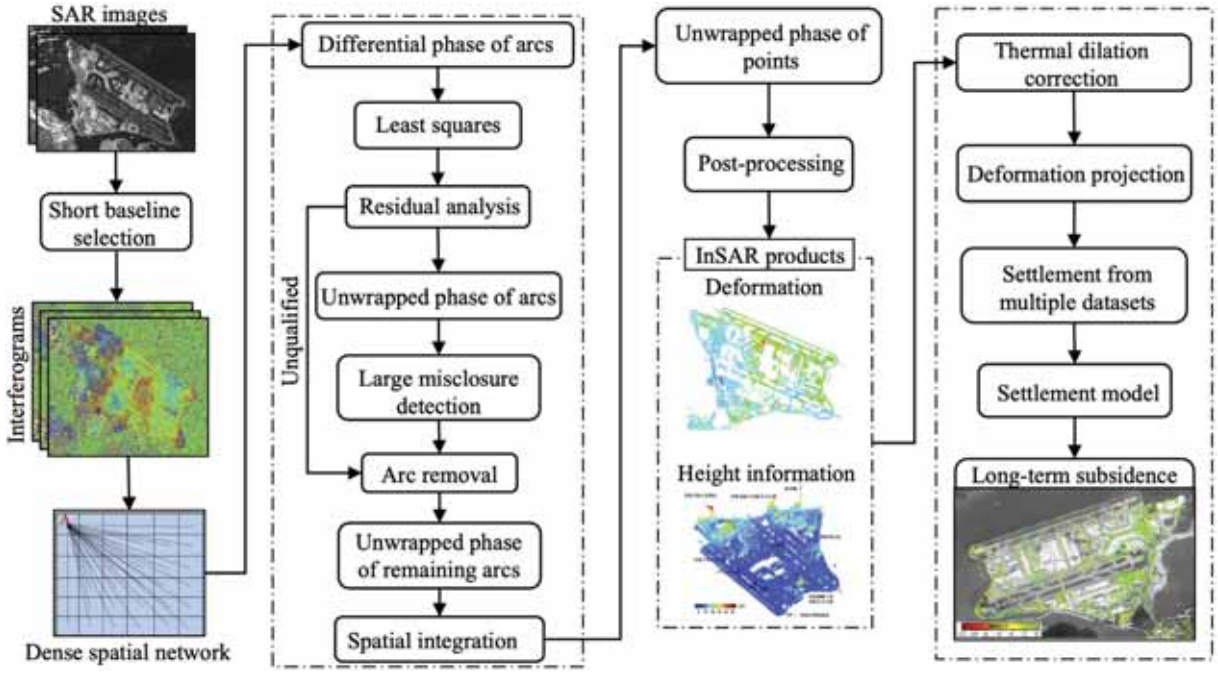

Fig. 4. Flowchart of data processing.

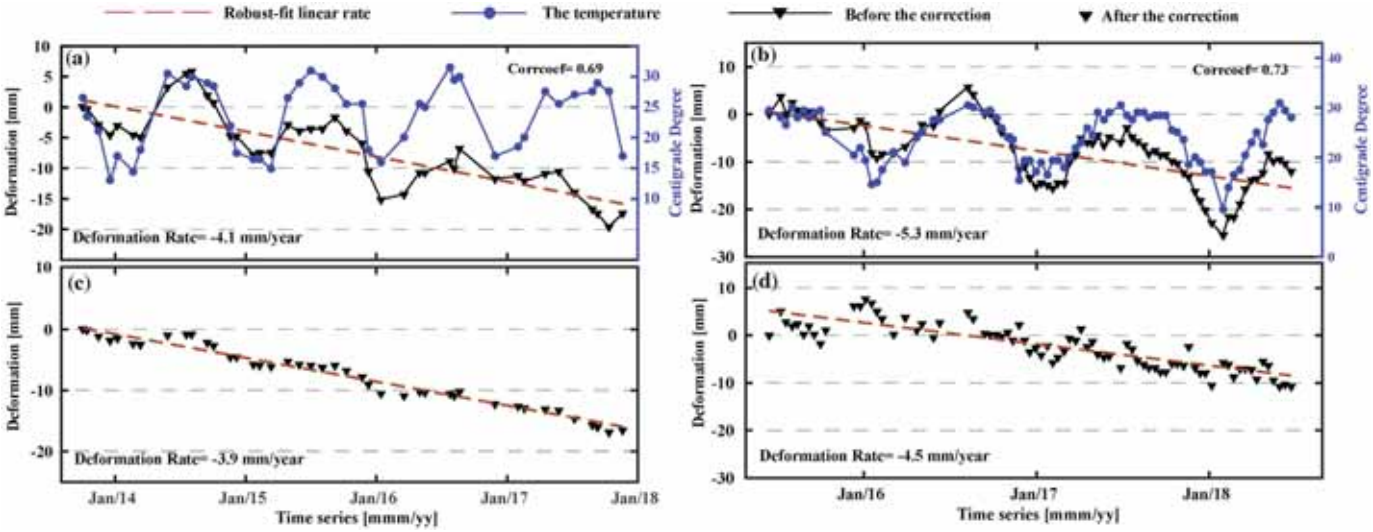

Fig. 5. Estimated deformation of two points on a building from CSK and Sentinel-1A datasets, respectively, (a), (b) before and (c), (d) after correcting for the thermal dilation effect.

decorrelation in any of the datasets, such as construction sites in the area, may be missed from the overall long-term settlement results.

4. Discussion

4.1. Accuracy validation

We use the results derived from data of the cross-heading tracks, i.e., 175, 297 and 25 in Fig. 6(c), (d), and (e) to cross-validate the results from the different ASAR datasets, similarly to Raucoules et al. (2009) and Jiang and Lin (2010). From visual inspection of the velocity maps estimated from the different ASAR datasets, very similar deformation patterns can be seen (see Fig. 6(c)-(e)), although the imaging geometries were different. To have a closer comparison, we convert the LOS deformation into vertical direction and resample the results into common 50 m grid to reduce the effect of the shift in geolocation. The correlation coefficients between the different results and the standard deviations of the differences are calculated. Fig. 8 gives the density scatterplots between the three sets of results. The correlation coefficients are 0.88, 0.91, and 0.85, respectively and the corresponding standard deviations are 1.79 mm/year, 2.41 mm/year, and 2.37 mm/year, indicating excellent agreements between the results.

Fig. 9(a) and (b) is the settlement velocity maps estimated from the CSK and Sentinel data, respectively. Again, the settlement patterns are very similar. To validate the results, we have compared the InSAR time series settlement with two leveling points (i.e., P1 and P2 shown in the figures) (Ma et al., 2019). In Fig. 9 (c) and (d), the results from both CSK and Sentinel data agreed well with the leveling measurements. The differences between them might relate to the uncertainty and effect of the atmospheric delays, decorrelation effect, and differences in location and time between the InSAR and leveling data (Schmidt and Bürgmann, 2003).

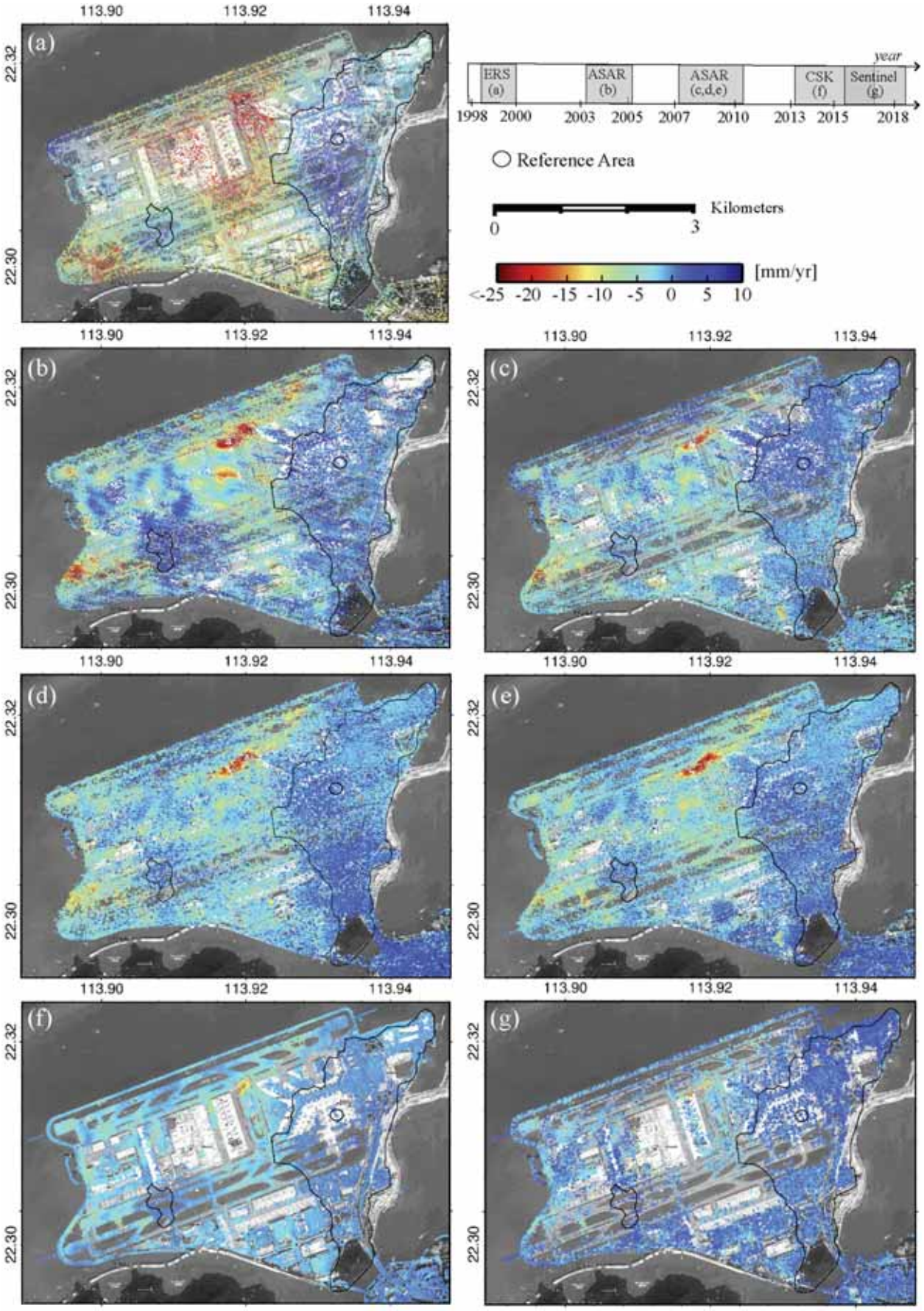

(caption on next page)

Fig. 6. LOS deformation velocity maps estimated from (a) ERS-2 descending, (b) ASAR descending (orbit 175, 2003–2005), (c) ASAR descending (orbit 175, 2007–2010), (d) ASAR ascending (orbit 25, 2007–2010), (e) ASAR ascending (orbit 297, 2007–2009), (f) CSK descending (2013–2017), and (g) Sentinel-1A ascending (2015–2018) SAR datasets. (Background image: Google Maps satellite image.)

In addition, a continuously operating GPS station located in the area, namely HKCL (see Figs. 1 and 10), is used to validate the accuracy of the estimated long-term settlement. The station belongs to the MAGNET geodetic network operated by the Nevada Geodetic Laboratory (Blewitt et al., 2018). The trend in the HKCL GPS measurements is first corrected with the mean deformation measurements of the other 12 GPS stations in Hong Kong (Fig. 10) for the effect of tectonic plate motion. The black and red vectors in Fig. 10 represent the deformation measurements at the stations, with and without the trend correction. The 3-D displacements of HKCL after the correction are plotted in the upper left panel of Fig. 10. The station was constructed in 2013. Therefore, only the deformation measurements from 2013 to 2018 are available.

Fig. 11 compares the settlement estimated from MT-InSAR (blue triangles) and calculated from the settlement model (line) with the GPS measurements (gray squares) at the HKCL station. The enlarged plot in Fig. 11(b) indicates that the model fits to the GPS measurements very well with a standard deviation of only 0.30 mm. In addition, the GPS and InSAR measurements agree with each other well at the station with a standard deviation of 1.09 mm.

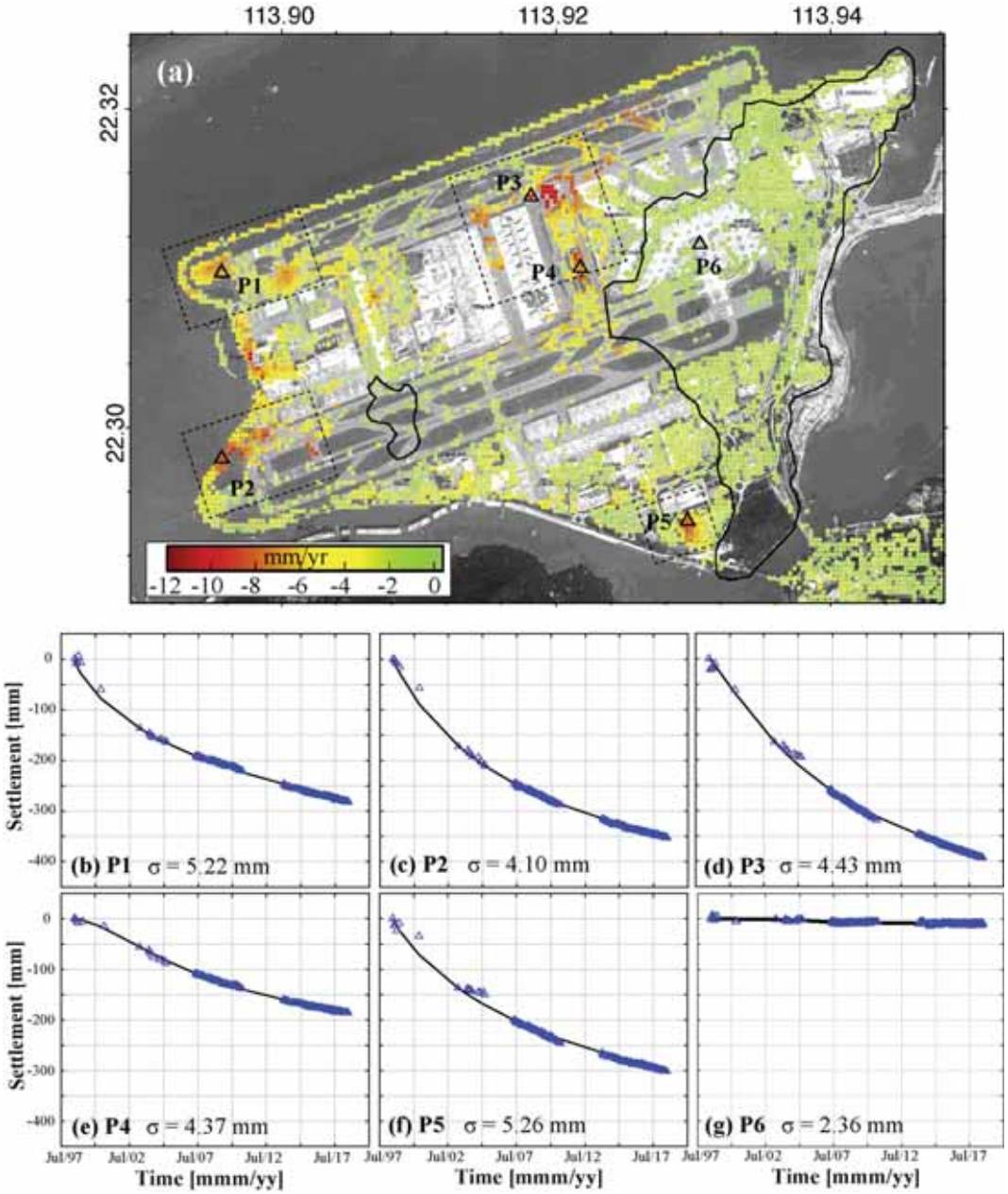

Fig. 7. (a) Estimated overall settlement velocity over the two decades. (b)-(g) Time series of settlements of six selected points estimated from MT-InSAR (blue triangles) and the settlement model (curves). (Background image: Google Maps satellite image). (For interpretation of the references to colour in this figure legend, the reader is referred to the web version of this article.)

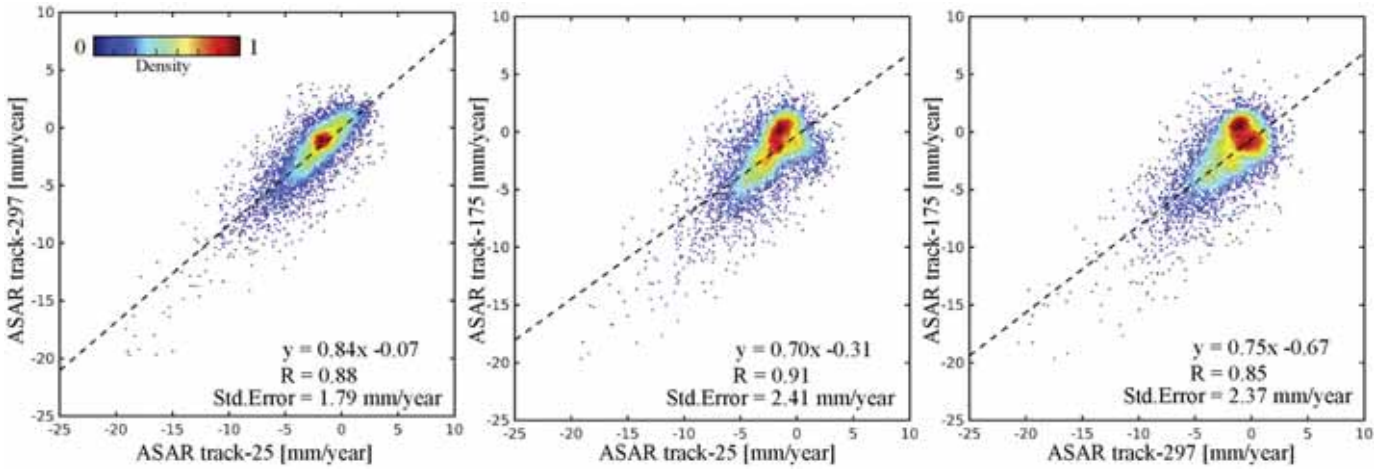

Fig. 8. Scatterplots of deformation velocity measurements from ASAR tracks 25, 297 and 175. The correlation coefficients are 0.88, 0.91, and 0.85, respectively and the corresponding standard deviations are 1.79 mm/year, 2.41 mm/year, and 2.37 mm/year.

4.2. Effect of neglecting the horizontal displacements

In computing the vertical displacements from the MT-InSAR line-of-sight measurements, the horizontal displacements were considered negligible. The LOS displacement (D_{los}) is a projection of 3-D displacement to the LOS direction,

$$D_{los} = d_v \cos(\theta) - d_e \cos(\beta) \sin(\theta) - d_n \sin(\beta) \sin(\theta) \quad (5)$$

where β is the azimuth angle of the satellite; θ is the radar incidence angle; and d_v, d_e, and d_n represent the displacements in vertical, eastern and northern directions, respectively.

When neglecting the horizontal displacements, it is assumed that $d_e = d_n = 0$. As seen in Fig. 10, the mean velocities in the eastern and northern directions at HKCL station are 0.33 mm/year and −0.28 mm/year, respectively, whereas the mean velocity of the vertical displacement is 1.35 mm/year. Therefore, the vertical displacement dominates. For example, when considering the ascending ENVISAT SAR data where $\theta = 23^{\circ}$ and $\beta = -12^{\circ}$, the contribution of the horizontal displacements to the LOS displacement is only about 0.15 mm/year. The error is considered acceptable in view of the settlement velocity of 1.35 mm/year.

We also estimate the displacements in the eastern and vertical

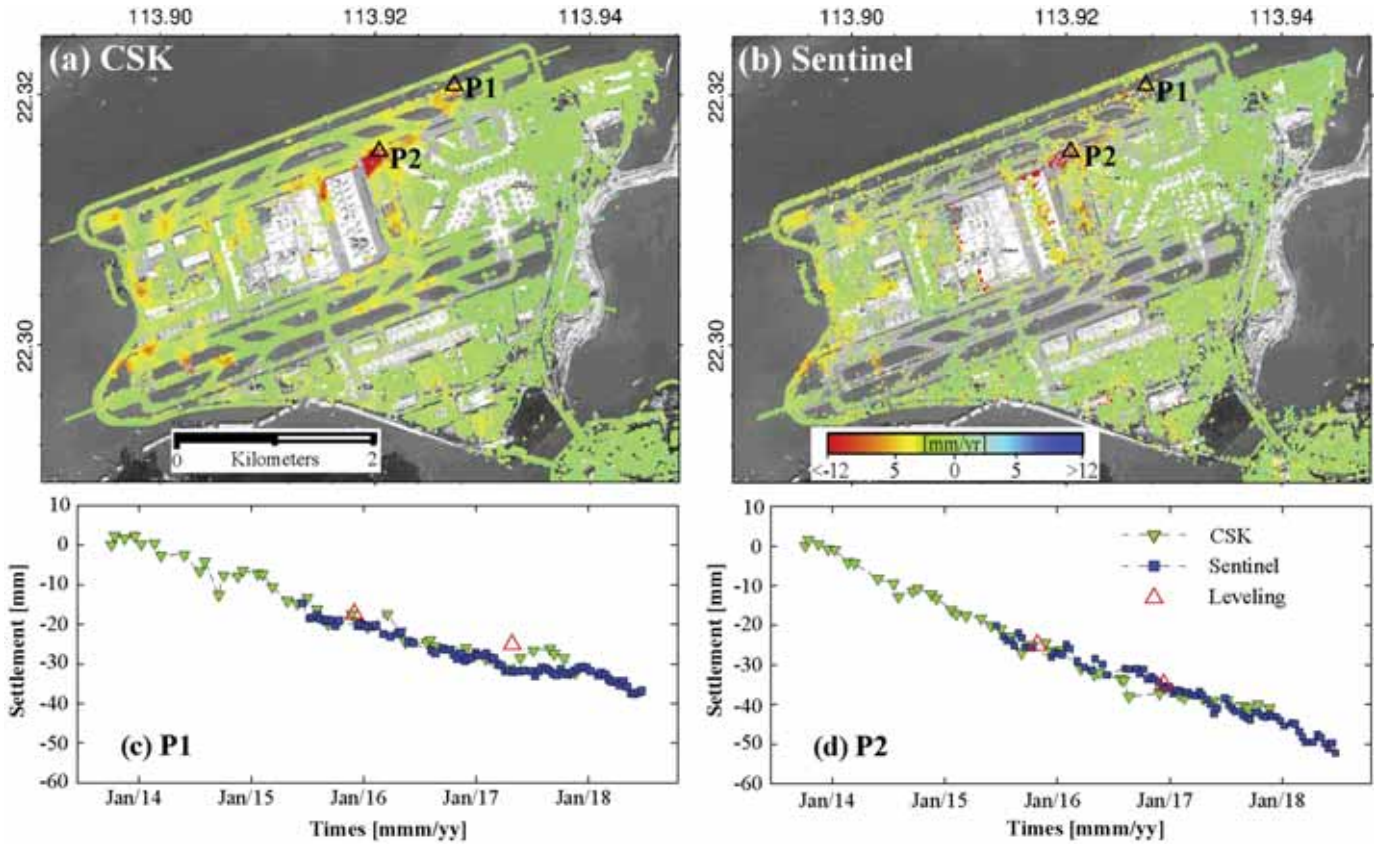

Fig. 9. Settlement velocity maps from (a) CSK (2013–2017) and (b) Sentinel (2015–2018) datasets, respectively. (c) and (d) are settlement histories of points P1 and P2 from InSAR and leveling. (Background image: Google Maps satellite image.)

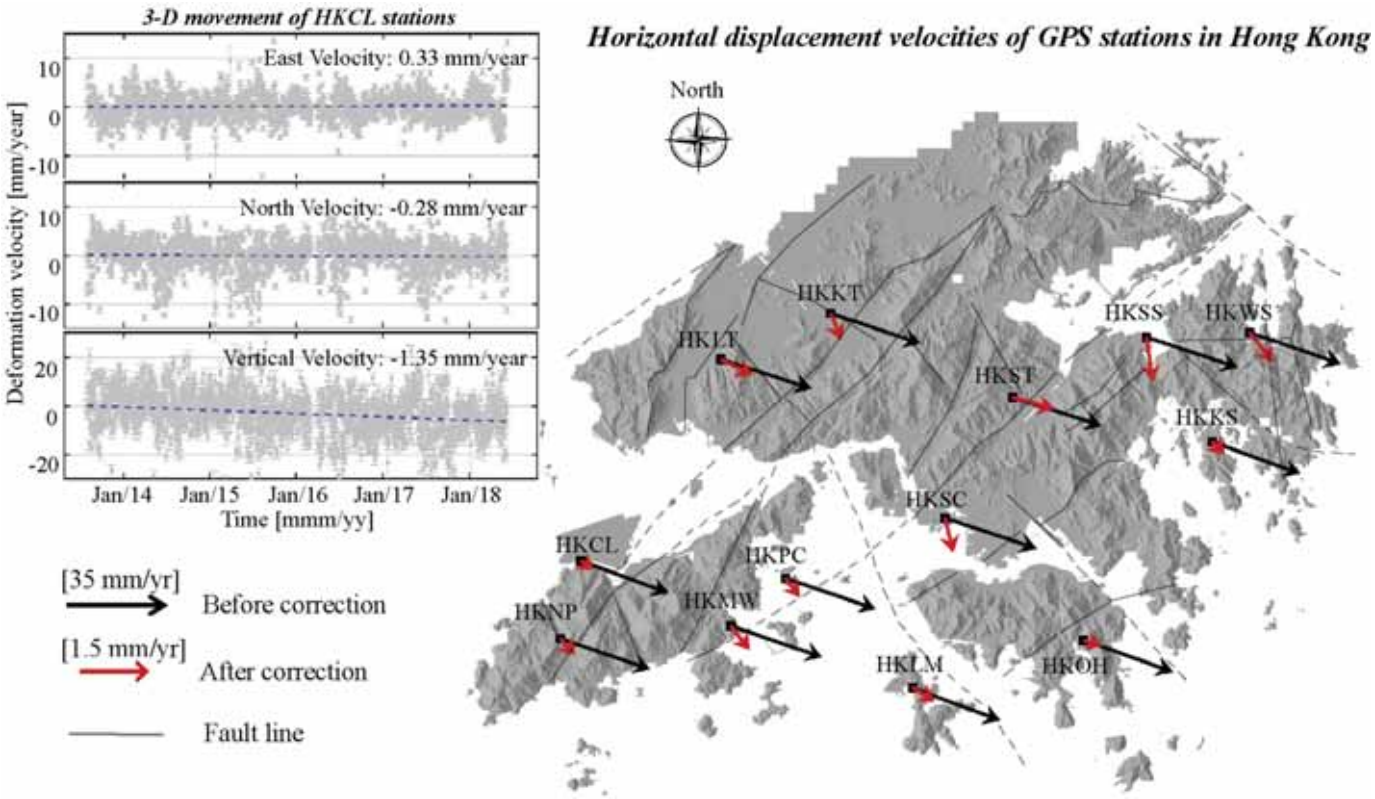

Fig. 10. Displacement vectors of 13 continuously operating GPS stations in Hong Kong before (black arrows) and after (red arrows) correcting the global motion trends. The left panel shows the 3-D displacements at the station after the correction. (For interpretation of the references to colour in this figure legend, the reader is referred to the web version of this article.)

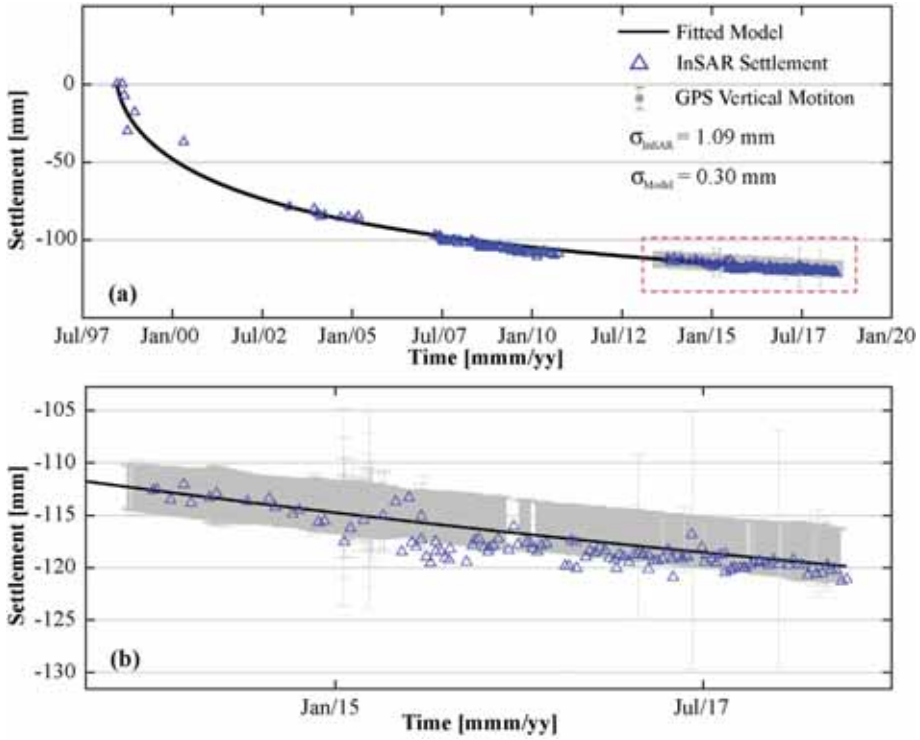

Fig. 11. (a) Settlement of HKCL station from GPS, InSAR and the settlement model. (b) Enlarged plot of the portion of (a) outline by the red rectangle. (For interpretation of the references to colour in this figure legend, the reader is referred to the web version of this article.)

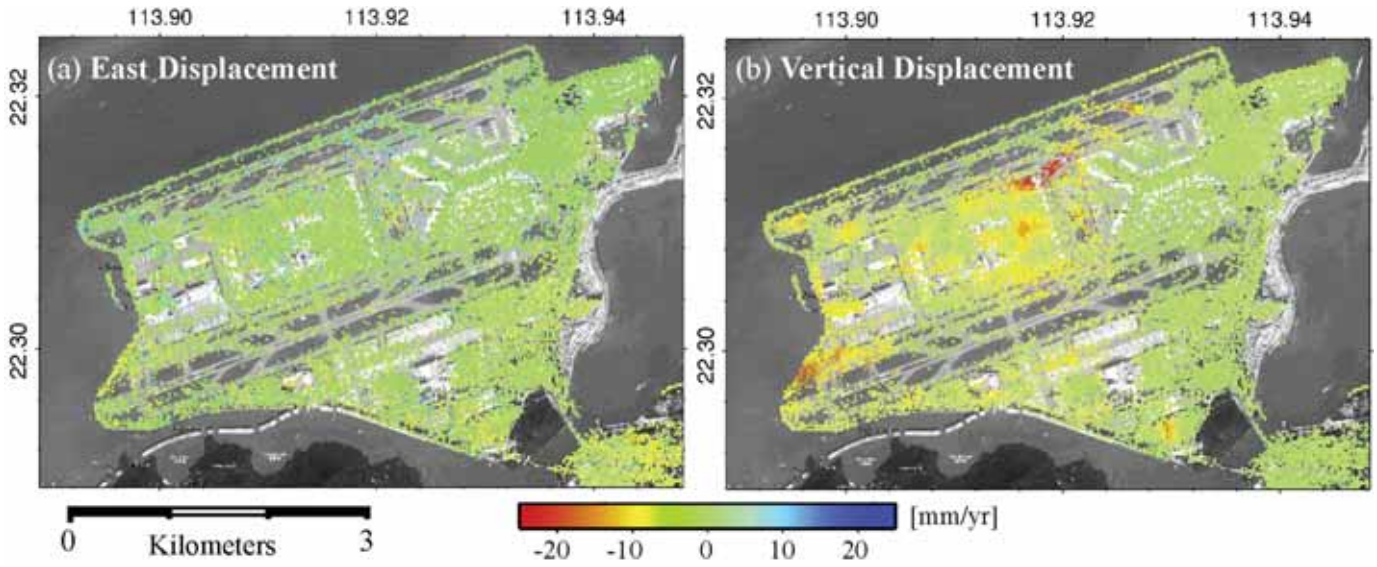

Fig. 12. The estimated mean displacement velocities in (a) eastern and (b) vertical directions. (Background image: Google Maps satellite image.)

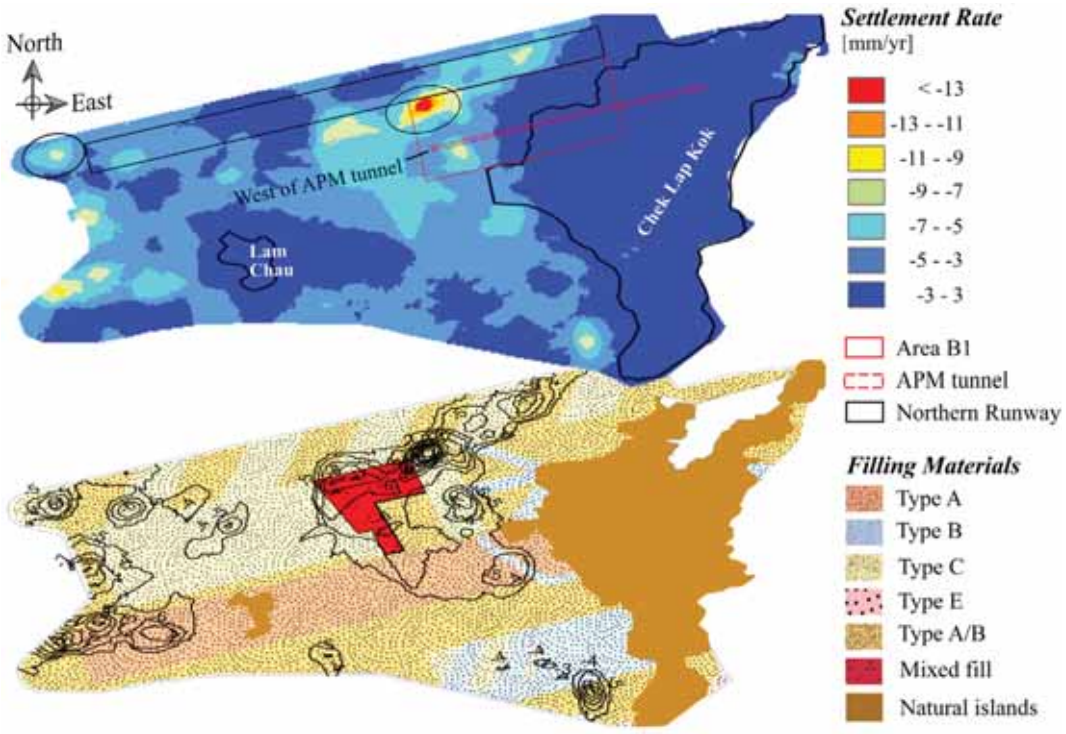

Fig. 13. Mean settlement velocity (after interpolation) and the approximate distribution of the different types of filling materials over the HKIA platform (Plant et al., 1998). The contour lines in the bottom panel illustrate the settlement rate with a contour interval of 1 mm/year.

directions based on the 2007–2010 ascending and descending ENVISAT ASAR data (see Fig. 3 and Fig. 6(c, d, e)). We first resample the displacements to a common geo-referenced grid of 20 m resolution, and then calculate the 2-D displacements based on the common points similarly to Fialko et al. (2001), Wright et al. (2004), and Hu et al. (2014). The estimated mean displacement velocities are shown in Fig. 12. The results also show that the vertical displacements are much more dominant than the horizontal displacements. Some localized anomalous values in the east-west direction may be due to resampling errors.

4.3. Contributing factors for the residual settlement of the HKIA

The spatiotemporal evolution of the HKIA settlement over the past two decades as revealed in the study is considered related to three main factors, the landfill materials, the underlying alluvial sediments, and the construction stages as discussed below.

4.3.1. Landfill materials

As described in Section 2.1, the HKIA platform was reclaimed with different landfill materials, namely, Types A-E, Type A/B, and mixed filling (see Table 1). Jiang and Lin (2010) have discussed the potential reasons for the settlement of the southern runway by analyzing the correlation between the measured settlement and the landfill materials.

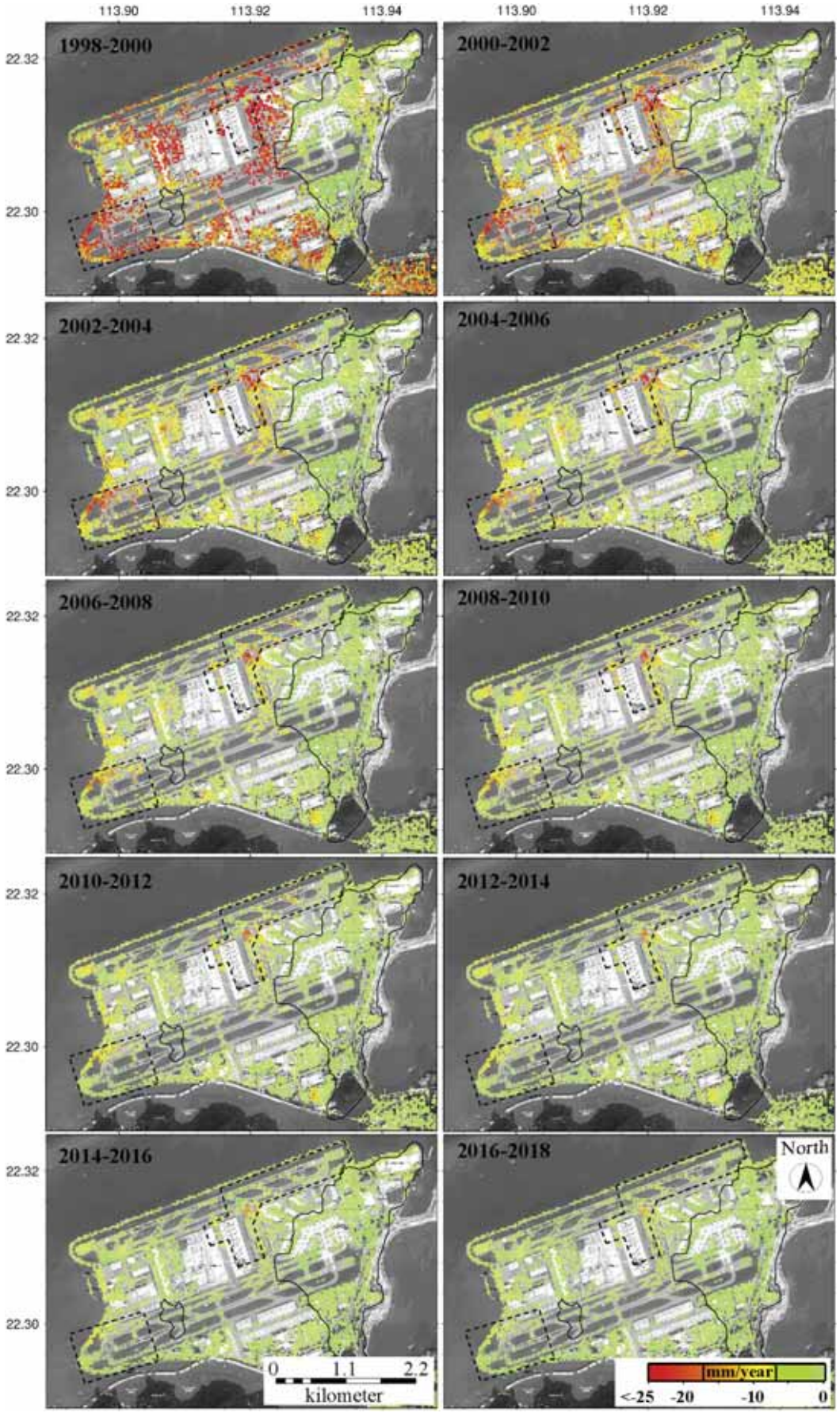

Fig. 14. Snapshots of settlement velocity calculated from the settlement model at two-year intervals. The dashed outlines show the areas reclaimed last. (Background image: Google Maps satellite image.)

Our results confirmed the findings of Jiang and Lin (2010) and provide more insights into the settlement of the northern runway. Fig. 13 shows the estimated mean settlement velocity (after interpolation with a Kriging interpolator (Oliver, 1990)) and the approximate distribution of the landfill materials. The main settlement areas are adjacent to the Chek Lap Kok island on the northwestern side, and at the western end of the platform. The largest settlement, with a magnitude of over 13 mm/year, occurred at the central part of the northern runway. The main settlement area seems to match well with the area reclaimed with the mixed filling material. According to Plant et al. (1998), the mixed filling material consists of material Types A/B, B and C and is thus quite variable in grading and compressibility. Therefore, it is very likely that the mixed filling material is responsible for the significant settlement. Plant et al. (1998) in fact suspected that the mixed filling material may cause significant settlement. This is the first time that the theory is confirmed through actual settlement measurements.

The construction of the Automated People Mover (APM) tunnel (marked by red dashed rectangle in Fig. 13) may have also affected the settlement pattern. According to Plant et al. (1998), part of the APM (a section of 675 m) was constructed in the reclaimed area (see Fig. 13). In addition, the area at the west end of the APM was filled with Type C filling material. The Type C material is composed of sand and has a larger creep compression rate than Type A/B and B materials (Plant et al., 1998). The area near the western end of the APM therefore suffered from significant settlement.

4.3.2. Underlying alluvial sediments

The underlying alluvial sediment may have accounted for some settlement in the western end and the middle section of the northern runway (the elliptic areas in Fig. 13). According to Plant et al., 1998, the two areas have the thickest underlying alluvial sediments. It was initially planned to treat specially the sediments before the construction of the northern runway to reduce the settlement. However, as the northern runway needed to be constructed earlier than previously scheduled, the planned special ground treatment for the underlying alluvium was abandoned, which has likely resulted in significant creep settlement in the areas.

4.3.3. Construction stages

The construction stages may have been responsible for the settlement in the western end of the southern runway, and the central section and eastern end of the northern runway. Fig. 14 shows the snapshots of the settlement velocity calculated from the settlement model at two-year intervals. The results indicate that the area that is northwest of the Chek Lap Kok island and the western end of the platform have experienced the most significant settlement since about 2003, i.e., after the primary consolidation. The two areas (outlined in Fig. 14), as described in Section 2.1, were last reclaimed. The finding agrees well with the prediction of Plant et al. (1998) and Tosen et al. (1998), and the results of Jiang and Lin (2010).

5. Conclusions

We have retrieved for the first time the full settlement history of the Hong Kong International Airport platform using data from multiple SAR sensors, an improved MT-InSAR method, and a settlement model. The results have demonstrated that the HKIA platform has experienced serious heterogeneous ground settlement over the past 20 years. The settlement appeared more uniform during 1988–2000 when the primary consolidation dominated. It then became heterogeneous and localized. The area that is adjacent to the Chek Lap Kok island on the northwestern side has experienced the most significant settlement and the accumulated settlement has reached 40 cm over the study period. Joint analysis of the measured settlement and geological data of the northern runway has indicated for the first time that the settlement may have been mainly associated with the fill materials, the alluvial deposits, and the construction stages.

The study has also shown that it is possible to use SAR data from multiple sensors to build a long deformation history, e.g., over two decades that exceeds the service life of any SAR satellites to date. It is also considered important to continuously monitor the deformation of important infrastructures like the HKIA with space-borne radar remote sensing techniques to ensure their safe working conditions.

Declaration of Competing Interest

The authors declare that they have no known competing financial interests or personal relationships that could have appeared to influence the work reported in this paper.

Acknowledgments

This work was supported in part by the National Natural Science Foundation of China under Grant 41774023, the Research Grants Council (RGC) of Hong Kong (PolyU152232/17E and PolyU152164/18E), the Research Institute for Sustainable Urban Development (RISUD) (1-BBWB). The authors would like to thank the Hong Kong Government for providing the high-resolution LiDAR DEM and the E-GEOS for providing the CSK SAR dataset under the science proposal ID 703.

Appendix A. Supplementary data

Supplementary data to this article can be found online at https://doi.org/10.1016/j.rse.2020.111976.

References

Bamler, R., Hartl, P., 1998. Synthetic aperture radar interferometry. Inver. Prob. 14 (4), R1.
Berardino, P., Fornaro, G., Lanari, R., Sansosti, E., 2002. A new algorithm for surface deformation monitoring based on small baseline differential SAR interferograms. IEEE Trans. Geosci. Remote Sens. 40 (11), 2375–2383.
Blewitt, G., Hammond, W.C., Kreemer, C., 2018. Harnessing the GPS data explosion for interdisciplinary science. Eos 99.
Chang, L., 2015. Monitoring Civil Infrastructure Using Satellite Radar Interferometry. Doctoral dissertation. Delft University of Technology, TU Delft.
Costantini, M., Falco, S., Malvarosa, F., Minati, F., Trillo, F., Vecchioli, F., 2014. Persistent scatterer pair interferometry: approach and application to COSMO-SkyMed SAR data. IEEE J. Sel. Topics Appl. Earth Observ. Remote Sens. 7 (7), 2869–2879.
Ding, X., Liu, G., Li, Z., Li, Z., Chen, Y., 2004. Ground subsidence monitoring in Hong Kong with satellite SAR interferometry. Photogramm. Eng. Remote Sens. 70 (10), 1151–1156.
Fattahi, H., Amelung, F., 2013. DEM error correction in InSAR time series. IEEE Trans. Geosci. Remote Sens. 51 (7), 4249–4259.
Ferretti, A., Prati, C., Rocca, F., 2000. Nonlinear subsidence rate estimation using permanent scatterers in differential SAR interferometry. IEEE Trans. Geosci. Remote Sens. 38 (5), 2202–2212.
Ferretti, A., Prati, C., Rocca, F., 2001. Permanent scatterers in SAR interferometry. IEEE Trans. Geosci. Remote Sens. 39 (1), 8–20.
Fialko, Y., Simons, M., Agnew, D., 2001. The complete (3-D) surface displacement field in the epicentral area of the 1999 Mw7. 1 Hector mine earthquake, California, from space geodetic observations. Geophys. Res. Lett. 28 (16), 3063–3066.
Hooper, A., Zebker, H., Segall, P., Kampes, B., 2004. A new method for measuring deformation on volcanoes and other natural terrains using InSAR persistent scatterers. Geophys. Res. Lett. 31 (23).
Hu, J., Li, Z., Ding, X., Zhu, J., Zhang, L., Sun, Q., 2014. Resolving three-dimensional surface displacements from InSAR measurements: a review. Earth Sci. Rev. 133, 1–17.
Hussain, E., Hooper, A., Wright, T.J., Walters, R.J., Bekaert, D.P., 2016. Interseismic strain accumulation across the central north Anatolian fault from iteratively unwrapped InSAR measurements. J. Geophys. Res. 121 (12), 9000–9019.
Jiang, L., Lin, H., 2010. Integrated analysis of SAR interferometric and geological data for investigating long-term reclamation settlement of Chek lap Kok airport, Hong Kong. Eng. Geol. 110 (3–4), 77–92.
Jiang, M., Ding, X., Tian, X., Malhotra, R., Kong, W., 2014. A hybrid method for optimization of the adaptive Goldstein filter. ISPRS J. Photogramm. Remote Sens. 98, 29–43.
Kampes, B.M., 2006. Radar Interferometry. Springer.
Liang, H., Zhang, L., Ding, X., Lu, Z., Li, X., 2018. Toward mitigating stratified tropospheric delays in multitemporal InSAR: A quadtree aided joint model. IEEE Trans.

Geosci. Remote Sens. 99, 1–13.
Liu, G., Ding, X., Chen, Y., Li, Z., Li, Z., 2001. Ground settlement of Chek Lap Kok Airport, Hong Kong, detected by satellite synthetic aperture radar interferometry. Chin. Sci. Bull. 46 (21), 1778–1782.
Ma, P., Wang, W., Zhang, B., Wang, J., Shi, G., Huang, G., Lin, H., 2019. Remotely sensing large-and small-scale ground subsidence: a case study of the Guangdong–Hong Kong–Macao Greater Bay Area of China. Remote Sens. Environ. 232, 111282.
Massonnet, D., Feigl, K.L., 1998. Radar interferometry and its application to changes in the Earth's surface. Rev. Geophys. 36 (4), 441–500.
Monserrat, O., Crosetto, M., Cuevas, M., Crippa, B., 2011. The thermal expansion component of persistent scatterer interferometry observations. IEEE Geosci. Remote Sens. Lett. 8 (5), 864–868.
Niu, F., Liu, M., Cheng, G., Lin, Z., Luo, J., Yin, G., 2015. Long-term thermal regimes of the Qinghai-Tibet railway embankments in plateau permafrost regions. Sci. China Earth Sci. 58 (9), 1669–1676. https://doi.org/10.1007/s11430-015-5063-0.
Oliver, M.A., 1990. Kriging: a method of interpolation for geographical information systems. Int. J. Geogr. Inform. Syst. 4, 313–332.
Pepe, A., Lanari, R., 2006. On the extension of the minimum cost flow algorithm for phase unwrapping of multitemporal differential SAR interferograms. IEEE Trans. Geosci. Remote Sens. 44 (9), 2374–2383.
Pepe, A., Bonano, M., Zhao, Q., Yang, T., Wang, H., 2016. The use of C-/X-band time-gapped SAR data and geotechnical models for the study of Shanghai's ocean-reclaimed lands through the SBAS-DInSAR technique. Remote Sens. 8 (11), 911.
Plant, G., Oakervee, D., 1998. Hong Kong International Airport-civil engineering design. In: Proceedings of the Institution of Civil Engineers-Civil Engineering. 126(5). Thomas Telford, pp. 15–34.
Plant, G.W., Covil, C.S., Hughes, R.A., 1998. Site Preparation for the New Hong Kong International Airport. Thomas Telford.
Raucoules, D., Bourgine, B., De Michele, M., Le Cozannet, G., Closset, L., Bremmer, C., Agudo, M., 2009. Validation and intercomparison of persistent Scatterers interferometry: PSIC4 project results. J. Appl. Geophys. 68 (3), 335–347.
Rosen, P.A., Hensley, S., Joughin, I.R., Li, F.K., Madsen, S.N., Rodriguez, E., Goldstein, R.M., 2000. Synthetic aperture radar interferometry. Proc. IEEE 88 (3), 333–382.
Schmidt, D.A., Bürgmann, R., 2003. Time-dependent land uplift and subsidence in the Santa Clara valley, California, from a large interferometric synthetic aperture radar data set. J. Geophys. Res. 108.
Sun, Q., Jiang, L., Sun, Y., Bai, L., Wang, H., 2016. Monitoring ground deformation in Hong Kong International airport with NL-InSAR filtering. In: Proceeding of the IEEE International Geoscience and Remote Sensing Symposium (IGARSS 2016), 10–15 July, Beijing, China, pp. 5978–5981.
Sun, Q., Jiang, L., Jiang, M., Lin, H., Ma, P., Wang, H., 2018. Monitoring coastal reclamation subsidence in Hong Kong with distributed scatterer interferometry. Remote Sens. 10 (11), 1738.
Tosen, R., Pickles, A., Jaros, M., 1998. Assessment of differential settlement at Chek Lap Kok Airport reclamation site. In: Proceedings of the A Seminar on the Geotechnical Aspects of the Airport Core Projects. Kong Institution Hongof Civil Engineers, Hong Kong, China.
Uiterwijk, F., 1994. Planning, Design, Tendering and Construction of the Chek Lap Kok Airport Platform. Waterbouw als exportprodukt grootschlige landaanwinning in Zuidoost-Azië. Waterbouwdispuut, Delft. pp. 35–46.
Werner, C., Wegmüller, U., Strozzi, T., Wiesmann, A., 2000. Gamma SAR and interferometric processing software. In: Proceedings of the Ers-envisat Symposium, Gothenburg, Sweden. vol. 1620. pp. 1620.
Wright, T.J., Parsons, B.E., Lu, Z., 2004. Toward mapping surface deformation in three dimensions using InSAR. Geophys. Res. Lett. 31 (1), L01607.
Wu, S., Zhang, L., Ding, X., Perissin, D., 2018. Pixel-wise MTInSAR estimator for integration of coherent point selection and unwrapped phase vector recovery. IEEE Trans. Geosci. Remote Sens. 57, 2659–2668.
Zhang, L., Ding, X., Lu, Z., 2011. Modeling PSInSAR time series without phase unwrapping. IEEE Trans. Geosci. Remote Sens. 49 (1), 547–556.
Zhang, L., Lu, Z., Ding, X., Jung, H.-S., Feng, G., Lee, C.-W., 2012. Mapping ground surface deformation using temporarily coherent point SAR interferometry: application to Los Angeles Basin. Remote Sens. Environ. 117, 429–439.
Zhang, L., Ding, X., Lu, Z., Jung, H.-S., Hu, J., Feng, G., 2014. A novel multitemporal InSAR model for joint estimation of deformation rates and orbital errors. IEEE Trans. Geosci. Remote Sens. 52 (6), 3529–3540.
Zhao, Q., Lin, H., Zhang, Y., Jiang, L., 2009. Application of ASAR PSI techonology to ground deformation detection in mega-cities of the Pearl River Delta region in China. In: Proceeding of 17th International Geoinformatics (2009), 12–14 August, Virginia, USA.
Zhao, Q., Lin, H., Gao, W., Zebker, H.A., Chen, A., Yeung, K., 2011. InSAR detection of residual settlement of an ocean reclamation engineering project: a case study of Hong Kong International Airport. J. Oceanogr. 67 (4), 415–426.